https://dx.doi.org/10.1016/j.apcatb.2023.122958

Highly dispersed nickel site catalysts for diluted CO_2 photoreduction to CO with nearly 100% selectivity

Shujie Liang[a,c], Xiaohui Zhong[a], Zuqi Zhong[a], Hong Deng[a,b]*, Wai-Yeung Wong[c]*

[a] School of Environment and Energy, Key Laboratory of Pollution Control and Ecosystem Restoration in Industry Clusters (Ministry of Education), Guangdong Provincial Key Laboratory of Solid Wastes Pollution Control and Recycling, South China University of Technology, Guangzhou, Guangdong 510006, China

[b] Guangdong Engineering and Technology Research Center for Environmental Nanomaterials, South China University of Technology, Guangzhou, Guangdong 510006, China

[c] Department of Applied Biology and Chemical Technology and Research Institute for Smart Energy, The Hong Kong Polytechnic University, Hung Hom, Hong Kong, China

* Corresponding author. E-mail address: **dengh2016@scut.edu.cn** (H. Deng).

* Corresponding author. E-mail address: **wai-yeung.wong@polyu.edu.hk** (W.-Y. Wong).

Abstract

Photoconversion of CO_2 into value-added fuels has aroused widespread interest; however, this process is significantly limited by the inefficient thermodynamics and sluggish reaction dynamics in the diluted CO_2. To circumvent these obstacles, we design a bipyridine-based polyimide polymer for anchoring single Ni site for diluted CO_2 photoreduction. The desired Ni single atomic catalysts achieve high generation activity of ~ 2262 μmol/h with apparent quantum efficiency (A.Q.E.) of 0.20% for CO_2-to-CO in 0.1 atm CO_2 pressure. No measurable H_2 is produced in the catalytic process, affording nearly 100% CO selectivity over water splitting. This superior activity and selectivity outperform most previous atomical catalysts. Mechanistic analyses elucidate that the highly dispersed Ni atoms act as active sites for effective CO_2 binding and activation, and stabilize the rate-determining step of intermediates for CO generation. This work discloses the relationship between catalytic properties and single atoms for efficient solar-driven diluted CO_2 reduction.

Keywords: single-atom Ni^{2+}; CO_2 photoreduction; diluted CO_2; highly selectivity; visible-light photocatalysis

1. Introduction

Excessive consumption of fossil fuels results in worldwide energy issues with ever-increasing atmospheric CO_2 concentration, which drastically restricts social development and endangers human survival.[1-3] CO_2 photoreduction is a feasible technique for the utilization of CO_2 into high-valued fuels to simultaneously mitigate the impact of energy and environmental problems.[4, 5] Although numerous efforts have been devoted into this area, there are still many critical bottlenecks restricting its practical applications. Due to the intrinsically thermodynamic stability of CO_2, the current CO_2 reaction process requires high activation energy with very low efficiency.[6] Meanwhile, the catalytic selectivity to targeted products greatly suffers from the sluggish kinetics including multiple electrons and protons transfer processes, such as competing water reduction reaction.[7, 8] In this setting, most reported works are carried out in a high-purity CO_2 condition in order to acquire the ideal catalytic activity and selectivity.[9-11] Considering the anthropogenic emission with a typical CO_2 concentration of less than 15% is the largest source of CO_2 pollution, direct photoreduction of the diluted CO_2 will be more desirable and economical regardless of the high energy-consumption purification process.[12, 13] Therefore, it is imperative to develop catalysts with adequate activity and selectivity to realize diluted CO_2 photoreduction.

Single atom catalysts (SACs) have sparked intense interest in catalysis due to their unique physicochemical property distinct from metal nanoparticles.[14-16] The atomically isolated active metal sites have demonstrated maximum atom-utilization efficiency and excellent selectivity in some catalytic reactions, which therefore affords opportunities for improving the performance of CO_2 reduction.[17-19] Xiong and coworkers reported a single Co atom catalyst on the partially oxidized graphene nanosheets via a simple thermal treatment process for visible-light driven CO_2, and the turnover number and frequency for CO production reached 678 and 3.77 min^{-1}, respectively.[20] Xiang et al. constructed a Ni SAC on g-C_3N_4 via a self-limiting method, and outlined the crucial role of the unsaturated Ni-N coordination for the enhancement of CO_2 adsorption and rate-determining step of intermediates for CO generation, thus exhibiting a comparable CO_2-to-CO generation rate of 8.6 μmol g^{-1} h^{-1} under visible light illumination.[21] Very recently, single Ni sites with special local coordination environment have also been reported for good catalytic activity and selectivity of CO_2 photoreduction due to the hydrogen-bond interactions between the keto nodes and the Ni-CO_2 reaction intermediate.[12] These unique merits indicate SACs have great potential for the photocatalytic CO_2 conversion, especially for the diluted CO_2 application.

In this present work, we develop a bipyridine-based polyimide polymer (Bpy-PDI) via condensation of the mixture containing 3,4,9,10-perylenetetracarboxylic dianhydride (PDA) with [2,2'-bipyridine]-5,5'-diamine (Bpy). Bpy-PDI contains the bipyridyl nitrogen atoms, which can act as the chelating sites to stabilize Ni atoms. Therefore, Ni ions were immobilized on Bpy-PDI by a facile hydrothermal process. We subsequently showed direct experimental evidence that single Ni atoms were incorporated into the targeted polymer. The local atomic coordination configuration of Ni SACs was thoroughly analyzed by extended X-ray absorption fine structure (EXAFS) and X-ray absorption near-edge structure (XANES), and directly imaged by annular dark-field scanning transmission electron microscope (HAADF-STEM). DFT calculations unambiguously determined their atomistic structures and correlation with photocatalytic activity towards the CO_2 photoreduction, especially for the diluted CO_2. This work points out new insights into the investigation of Ni-based catalysts for efficient diluted CO_2

photoreduction.

2. Experimental section

2.1. Chemicals

3,4,9,10-Perylenetetracarboxylic dianhydride (PDA), [2,2'-bipyridine]-5,5'-diamine (Bpy), benzidine (BA), imidazole, anhydrous zinc acetate, acetonitrile (MeCN), and triethanolamine (TEOA) were obtained from Aladdin Industrial Corporation. Dimethyl sulfoxide (DMSO), dimethylformamide (DMF), $[Ru(bpy)_3]Cl_2{\cdot}6H_2O$ (bpy = 2′2′-bipyridine) and nickel chloride hexahydrate ($NiCl_2{\cdot}6H_2O$) were purchased from Shanghai Sinopharm Chemical Reagents, China. All chemicals were used in this experiment without further purification. Deionized water (18 MΩ·cm) was used throughout the experiments.

2.2. Synthesis of materials

Synthesis of Bpy-PDI. Bpy (0.372 g, 2 mmol), PDA (0.78g, 2 mmol), and anhydrous zinc acetate (0.555 g) were added into a 500 mL three-necked flask containing 5.0 g of imidazole and then refluxed under 140 °C for 48 hours. After cooling to room temperature, 250 mL of 1 mol L^{-1} HCl was added into the mixture, which was stirred for several hours until no further precipitate was detected. The precipitate was retrieved by vacuum filtration and washed with DI water in order to remove the Cl^- impurity. Subsequently, the collected precipitate was washed with DMSO until the washings became colorless. Finally, the highly insoluble dark red product of Bpy-PDI was washed by EtOH and dried.

Synthesis of Bpy-PDI. BA-PDI was synthesized in the presence of BA rather than Bpy as the initial monomer. The experimental procedures were the same as for Bpy-PDI.

Preparation of Ni SACs. $NiCl_2{\cdot}6H_2O$ (50 mg) was placed in a flask and dissolved in 50 mL DMF. Bpy-PDI (200 mg) was dispersed into the solution with the assistance of ultrasound and the mixture was stirred at room temperature for 12 h. The precipitate was collected by vacuum filtration, and then washed three times with water and ethanol. The collected sample was dried overnight under vacuum in an oven at 60 °C and named as Ni SACs.

Contrast sample of BA-PDI-Ni was synthesized in a way similar to the above process except for the substrate material, which was BA-PDI here.

2.3. Characterization

Sample crystallinity was determined by X-ray diffraction (XRD) patterns using Cu-Kα radiation (λ=1.54178 Å) on a Bruker D8 Advance Powder X-ray diffractometer with operation conditions of 5° to 80° at 40 kV and 40 mA. X-ray photoelectron spectra (XPS) were performed using an Escalab 250Xi (Thermo Fisher Scientific) with C 1s binding energy as the reference. A Nicolet (thermos Nicolet Nexus) 670 FTIR spectrometer with KBr as the diluents was employed to collect the Fourier transform infrared (FTIR) spectra. UV–vis diffuse reflectance spectra (DRS) were performed by a UV 2600 spectrometer (Shimadzu, Japan) equipped with an integrating sphere using $BaSO_4$ as the reference. Morphological characterization was observed using a field emission scanning electron microscope (FE-SEM, SU8100, Hitachi). Aberration-corrected high-angle annular dark-field scanning TEM (HAADF-STEM) was performed using a JEOL ARM200F equipped with double aberration correctors and a cold field emission gun operated at 80 kV. The photoluminescence (PL) spectra were investigated using an Edinburgh FL/FS900 spectrophotometer. Brunauer–Emmett–Teller (BET) surface areas were conducted by N_2 adsorption/desorption measurements using a Micromeritics ASAP 2020 analyzer at 77 K. The pore size distribution was determined using the Barrett-Joyner-Halenda (BJH) method. The CO_2 adsorption isotherms were analyzed by the Micromeritics ASAP 2020 at 298 K. Photochemical tests were performed on a CHI 760E electrochemical workstation (Chenhua Instrument, Shanghai, China) to explore the photoelectrochemical performance in the CO_2 photoreduction process. The measurements were performed in a conventional three-electrode system with the working electrode, Pt plate as the counter electrode, and Ag/AgCl electrodes as the reference electrode, respectively. The cyclic voltammetry (CV), Mott-Schottky plot (M-S), and linear sweep voltammetry (LSV) were performed in CO_2-saturated or Ar-saturated 0.1 M Na_2SO_4 electrolyte at a scan rate of 10 mV s^{-1}. All the samples were ground and uniformly daubed on the special adhesive tape and the raw XAS data were collected from the Beijing Synchrotron Radiation Facility at 1W1B. The storage ring energy is 2.5 GeV with current between 160 and 250 mA. Ni K-edge EXAFS was collected by fluorescence mode with appropriate absorption edge jump in the range from 8137 eV to 9122 eV. The acquired XAS data were analyzed by standard procedures with the ATHENA and ATHENA program in IFEFFIT software.[22] In situ FTIR measurements were performed by FT-IR spectrometer (Nicolet iS50 Thermo Scientific, USA). The reaction system was firstly treated by an Ar gas for 1 hour in dark to remove impurities, followed by passing the CO_2 and H_2O gas mixture for 30 min. Finally, the catalytic system was driven by Xe lamp and the in situ FTIR signals were collected within the given time.

2.4. Computational Methods

All the theoretical calculations with spin polarization were carried out using the Vienna Ab Initio Simulation Package (VASP).[23] The electron ion interaction was described with the projector augmented wave (PAW) method,[24] while the electron exchange and correlation energy were solved within the generalized gradient approximation with the revised Perdew-Burke-Ernzerhof (RPBE) exchange-correlation functional[25, 26]. To describe van der Waals interaction, the empirical correction in Grimme's method (DFT+D3) was used.[27] All geometries were fully optimized with a plane wave energy cutoff of 500 eV and the convergence criterion for the residual forces and total energies were set to be 0.03 eV/Å and 10^{-5} eV, respectively.

The theoretical model was constructed based on the experimental information, containing 6 N atoms, 8 O atoms, 58 C atoms, 24 H atoms, and 1 Ni atom. Note that the N atoms on both sides were passivated by H atoms. The lattice parameters were set as a = 50 Å, b = c = 20 Å, which is sufficient to minimize the interaction between periodic images. The 1×1×1 Gamma-centered k-point mesh was used to sample the Brillouin zone.

The Gibbs free energy change (ΔG) of each elementary step during the CO_2 electroreduction was calculated by using the computational hydrogen electrode (CHE) model proposed by Nørskov et al.[28] In this model, the chemical potential of the proton-electron pair in aqueous solution is related to that of one-half of the chemical potential of an isolated hydrogen molecule. The ΔG value can be obtained by the formula: $\Delta G = \Delta E + \Delta ZPE - T\Delta S$, where ΔE is the reaction energy of reactant and product species adsorbed on the catalyst directly obtained from DFT calculations; ΔZPE and ΔS are the changes between the adsorbed species and the gas phase molecules in zero-point energies and entropy at 298.15 K, which can be calculated from the vibrational frequencies.

The adsorption energy (E_{ads}) of CO_2 and H_2O molecules on the catalysts was calculated based on the equation: $E_{ads} = E_{total} - E_{catalyst} - E_{adsorbate}$, where E_{total}, $E_{catalyst}$, and $E_{adsorbate}$ represent the total energies of the systems containing the catalyst and adsorbate, the catalyst, and the adsorbate, respectively. According to this definition, a more negative adsorption energy indicates a stronger interaction.

2.5. Photocatalytic experiments

The photocatalytic experiments were carried out following reported procedures.[6, 7] In a quartz tube (60 mL), catalyst (1.0 mg) was dispersed in the mixing solution containing acetonitrile (3 mL), H_2O (2 mL), triethanolamine (1 mL) and $[Ru(bpy)_3]Cl_2{\cdot}6H_2O$ (abbreviated as Ru, 7.5mg) by ultrasound. This mixture system was evacuated and bubbled with highly purified CO_2 (99.999%) three times to absolutely remove the dissolved air, and filled with CO_2 with a value of one atmosphere. Photocatalytic tests were conducted in a PCX50B Discover multi-channel parallel photocatalytic reaction system (Perfect Light Co., Ltd.) with a 5 W white LED light ($400\ nm \leq \lambda \leq 800\ nm$). The photocatalytic products were determined and analyzed by gas chromatography (GC-7890B, Agilent). The gas products of CO and H_2 were identified and analyzed by FID detector and TCD detector, respectively.

The selectivity for CO_2-to-CO photoconversion was calculated as follows:

$$Selectivity\ of\ CO = \frac{n_{co}}{n_{co} + n_{H_2}}$$

The apparent quantum efficiency (A.Q.E.) for CO evolution was measured under photocatalytic reaction condition with a monochromatic 420 nm bandpass filter. The light intensity at 420 nm was measured to be $32.3\ mW{\cdot}cm^{-2}$ by an optical power meter (Ushio spectroradiometer, USR40). The illuminated area was estimated to be $3.0\ cm^2$. A.Q.E. was calculated using the following equation:

$$A.Q.E. = \frac{number\ of\ reacted\ electrons}{number\ of\ incident\ electrons}$$

$$= \frac{number\ of\ generated\ CO\ molecules\ \times 2}{number\ of\ incident\ electrons}$$

3. Results and discussion

3.1. Materials synthesis and characterizations

Polyimide polymers were synthesized by coupling 3,4,9,10-perylenetetracarboxylic dianhydride (PDA) with [2,2'-bipyridine]-5,5'-diamine (Bpy) and benzidine (BA), which were named as Bpy-PDI and BA-PDI, respectively (Fig. 1a and Fig. S1). Considering the strong interaction of the bipyridyl nitrogen and transition metal ions, nickel atoms can be easily anchored into the structure of Bpy-PDI. As shown in Fig. 1b, the disappearance of N-H vibrational signals (3466 and 3329 cm^{-1}) in Bpy and the stretching vibration of C=O (1770 cm^{-1}) in PDA directly indicated the formation of polymers by dehydration reaction. Out of the strong electronegativity and the conjugation effect, the C=O groups presented an obvious shift in the peak position to 1683 cm^{-1} in the Bpy-PDI polymer.[29] The crystallinity of Bpy-PDI was rather lower than that of BA-PDI, which may be attributed to the interaction of Zn ions with Bpy during the polymerization process (Fig. S2). No new crystalline phase could be observed in the Ni SACs (Fig. 1c), which precluded the formation of new crystal phases during the modification of Ni atoms. Negligible characteristic signals of residual zinc ions can be found in the XPS survey, indicating that the zinc ions were completely removed after sufficiently rinsing with acid (Fig. S3). The N 1s XPS spectra (Fig. 1d) for the Bpy-PDI sample presented two peaks: the 398.8 eV peak can be attributed to the pyridyl nitrogen species, while the 399.9 eV peak was characteristic of the imino nitrogen[30]. The binding energy of pyridyl nitrogen obviously disappeared in Ni SACs compared to that in Bpy-PDI, indicating the complexation of pyridyl nitrogen with the Ni ions, which was in line with the FTIR results (Fig. S4). Significant signals of Ni inferred the existence of Ni in the Ni SACs (Fig. 1e). High-resolution Ni 2p spectrum discerned the binding energies of Ni 2p1/2 and Ni 2p3/2 at 873.0 and 855.2 eV with shake-up satellite peaks (879.6 and 860.8 eV), which demonstrated that Ni ions were in +2 valence state. These results suggested that strong interactions existed between the Ni atoms and bipyridine moieties in the Ni SACs.

Supplementary Fig. S5 showed the morphology evolution of Bpy-PDI and Ni SACs, with no detectable nanoparticle phase of nickel. The high-resolution TEM image confirmed the absence of Ni nanoclusters (Fig. 2a-b). Aberration corrected high-angle annular dark-field scanning transmission electron microscopy (HAADF-STEM) with sub-Å resolution was then employed to elucidate the atomically dispersed nature of Ni atoms. A large amount of brighter spots, which were highlighted by yellow circles, could be directly monitored in Fig. 2c. The sizes of the spots were ~1.5 Å, which can be identified as Ni single atoms in Ni SACs. Energy-dispersive X-ray spectroscopy (EDS) confirmed the existence of C, N, O, and Ni elements (Fig. S6). Elemental mapping pictures revealed the highly homogeneous dispersion of randomly distributed four kinds of metal signals (Fig. 2d-h). Inductively coupled plasma optical emission spectroscopic (ICP-MS) testing disclosed the atom percent content of single Ni sites in Ni SACs sample was about 1.87 at. %, which was in line with XPS and EDS results (Table S1).

The Ni local environment at the atomic level was investigated by synchrotron X-ray absorption spectroscopy (XAS). As shown in Fig. 3a, the absorption edge position of Ni SACs was close to that of NiO and $NiCl_2$, which suggested that the valence state of Ni in Ni SACs was close to +2. As shown in Fig. 3b, only one dominated peak at ~ 1.6 Å for Ni SACs was examined in the Fourier-transformed (FT) k^2-weighted EXAFS spectrum. The Ni-Ni peak of Ni foil standard at ~2.2 Å and Ni-O-Ni peak of NiO standard at 2.5 Å were not detected in Ni SACs, precluding the aggregation of Ni-related oxides and clusters. Given the solid XPS evidence that Ni atoms were coordinated with N atoms, we excluded the possibility of Ni-N bond in Ni SACs. In reference to NiPc and $NiCl_2$, the first core shell of Ni SACs was located between that of the Ni-N and Ni-Cl. According to the previous report, the Ni center in Ni SACs may be in a planar geometry completed by two chlorides and two N atoms from one Bpy ligand[31]. Wavelet transform (WT)-EXAFS as a powerful tool was applied to investigate the atomic configuration of Ni SACs. As depicted in Fig. 3c, the WT-EXAFS signal for Ni SACs just depicted a maximum located at 4.0 $Å^{-1}$ assigned to the Ni-N/Cl contribution. No intensity maximum belonging to Ni-Ni and Ni-O can be observed, compared with its references of Ni foil and NiO. In line with the above HAADF-STEM results, all Ni species were atomically dispersed without detectable aggregation. These analyses provided strong evidence for the isolated feature of Ni species in Ni SACs.

3.2. Photocatalytic performance for CO_2 reduction

On the basis of the above high-content single nickel sites, as-prepared Ni SACs were applied to measure the photocatalytic performance of CO_2 reduction. The whole catalytic process was conducted in a mixture of MeCN/H_2O/TEOA, in which Ru acted as the photosensitizer. MeCN and H_2O were used as the aprotic and protic solvents, which were beneficial for CO_2 solubilization and promoted the reaction kinetics, respectively.[6, 32] Firstly, an experiment was performed to assess the content effect of Ni SACs on the CO_2 photoreduction in the pure CO_2 (Fig. 4a). Only CO and H_2 could be detected without any other hydrocarbon products at the same time, which was consistent with previous reports.[33, 34] The input amount of the catalyst played an important role on the catalytic properties. The yield of the CO was improved with the increase of Ni SACs content. When 1.5 mg of Ni SACs was used, the generation rate of CO reached the highest value of 3353.0 μmol/h. With the content of Ni SACs further increasing, the CO generation rate decreased. This phenomenon can be illustrated by the light-shielding effect caused by the excessive catalysts during the reaction process. Notably, the catalytic selectivity for CO was higher than 93.7% at 1.0 mg, and reached the optimal value of 100% when the catalytic input amount was over 1.5 mg. Therefore, the optimal usage dose of 1.5 mg with best photocatalytic performance was used in the following tests.

Control experiments were conducted to confirm the mechanism and details of the catalytic reaction (Fig. 4b). The generation rate of Bpy-PDI for CO product was 62.2

μmol/h. With the aim of the single Ni sites, Ni SACs exhibited a CO generation rate of 3353.0 μmol/h, which was 53-fold higher than that of Bpy-PDI. Similarly, BA-PDI-Ni presented a higher production rate of CO than that of BA-PDI, further indicating the crucial role of Ni catalytic site. It was worth noting that Ni SACs showed more excellent catalytic activity than that of BA-PDI-Ni. Although Ni SACs and BA-PDI-Ni had similar structures, the Ni SACs has a unique bipyridine motif, which was considered as the anchoring sites for loading more Ni atoms to trigger CO_2 photoreduction. No CO products could be inspired in the absence of TEOA, indicating that the sacrificial agent played an important role in accelerating the whole reaction. When there was no photosensitizer of Ru or irradiation, the CO_2-to-CO conversion was completely terminated, which inferred that the CO_2-to-CO reduction was a light-driven process.[35] The participation of CO_2 in the catalytic process was investigated by replacing CO_2 with Ar under identical photocatalytic reaction conditions. No CO was observed except for H_2, inferring that the CO product was originated from the CO_2 molecules. In order to further preclude unidentified photochemical decomposition of organics to yield CO products, isotope labeling tests by using $^{13}CO_2$ as carbon feedstock were carried out by gas chromatography-mass spectrometry (Fig. 4c and Fig. S7). Only ^{13}CO signals at $m/z = 29$ can be detected in the collected gas products when $^{13}CO_2$ was employed as the carbon source, indicating that the carbon source of CO was exclusively from CO_2.

In addition, the generation rate of CO was in line with the optical wavelength of the photosensitizer. Meanwhile, the quantum efficiency of Ni SACs was 0.30% at 420 nm, 0.26% at 450 nm, and 0.16% at 485 nm (Fig. S8). The trend of A.Q.E. correlated well with the optical absorption of the photosensitizer, suggesting that the CO-production activity of Ni SACs was initiated from the excitation of photosensitizer by light during the catalytic process.

According to the above analyses, we learned that Ni SACs presented impressive catalytic performance in pure CO_2. Considering the non-economical purification of low-concentration CO_2 (5-15% atm in N_2) in anthropogenic gas, direct transformation of diluted CO_2 into valuable chemicals may be more practical.[36] Therefore, the photocatalytic activity of Ni SACs was evaluated by monitoring CO production in different concentrations of diluted CO_2. The average generation rate and selectivity of CO were up to 2262 μmol/h and 100%, along with a high A.Q.E. of 0.2% in 0.1 atm CO_2 (Fig. 4d). Meanwhile, the CO generation rate achieved 2007 μmol/h with 94.2% CO selectivity in 0.05 atm. To the best of our knowledge, this superior CO generation rate and selectivity outperformed those in most current reports (Table S2 and S3). So, our work completed diluted CO_2 photoreduction with high catalytic activity and selectivity from 0.05 atm to 1.0 atm, which shed light on the possible utilization of CO_2 as a carbon source from anthropogenic gas without any other operation of concentration.

Long-term stability of CO_2 photocatalysts was an important parameter for their application. As shown in Fig. S9, the CO yield increased with the illumination time in 0.1 atm, and the accumulated CO yield reached 6771 μmol in four hours; however, the catalytic rate gradually decreased as the reaction progressed. Notably, the catalyst was reactivated after reintroducing an equal amount of the fresh photosensitizer into the system, confirming that the catalyst deactivation was due to photosensitizer consumption rather than the CO poisoning of the catalyst. To investigate the recyclability of the as-prepared Ni SACs, the used samples were recovered and reused for another three times in the fresh catalytic solution under the identical conditions. Fig. S10a demonstrated the stability of the Ni SACs catalyst in each periodical cycle, and an obvious deactivation of accumulated CO yield was hardly perceptible. The identical XRD patterns of fresh and used samples precluded structure collapse or phase changes during the photocatalytic process (Fig. S10b). Meanwhile, SEM images indicated that Ni SACs catalyst remained their original morphology without any metallic clusters or nanoparticles (Fig. S10c-d). These results confirmed the extraordinary stability of Ni SACs, which can be attributed to the firm coordination of Ni atoms with the bipyridyl nitrogen in the Ni SACs.

3.3. Catalytic mechanism study

The optical absorption properties of the Ni SACs and its counterparts were characterized by UV-vis-NIR diffuse reflectance spectra (DRS). As shown in Fig. 5a, PDA molecules showed a visible light absorption edge at 655 nm. PDA derived materials retained the visible light absorption properties of PDA, showing clearly optical absorption range between 400 and 900 nm, which implied that these catalysts can respond well to visible light irradiation. After polymerization, obviously enhanced absorption bands centered at 653 nm and redshifted to 665 nm occurred in Bpy-PDI, which may be originated from the conjugation effect of PDA and Bpy molecules.[29] Interestingly, the absorbance of Ni SACs showed an obvious extension with enhanced absorption intensity in the visible-light region ranging from 432 to 643 nm compared with Bpy-PDI, which could be observed directly with their dark red color changed from red-brown, due to the modified Ni ions embedded bipyridine both enhancing electron delocalization in the donor parts and promoting aggregation in the acceptor parts.[37] The light absorption capability of photocatalyst was a crucial factor for photocatalysis and thus Ni SACs catalysts were expected to occupy a favorable position with better photoactivity toward the target reaction.

As the band edge positions of the semiconductor played a crucial role in photocatalytic performance, the band gap and energy levels were determined.[38] According to the transformed differential spectra of Tauc plot, the optical energy band gaps of the PDA, Bpy-PDI, and Ni SACs were estimated to be about 1.73, 1.89, and 1.93 eV, respectively (Fig. 5b). The flat-band potential (E_{fb}) of Ni SACs in the Mott-Schottky plot was estimated to be -0.95 V vs. Ag/AgCl electrodes (-0.75 V *vs.* NHE, pH = 7) (Fig. 5c). The positive slope of the plot indicated Ni SACs was a kind of n-type semiconductor. As the lowest unoccupied molecular orbital (LUMO) edge of n-type semiconductor was more negative by about 0.10 V than that of E_{fb}.[39, 40] The LUMO can be estimated to be -0.85 V *vs.* NHE at pH = 7 for Ni SACs (Fig. 5d), which was higher than the redox potential of E (CO_2/CO) = −0.53 V (vs. NHE, pH = 7), and lower than that of the E ($Ru(bpy)_3^{2+*}/Ru(bpy)_3^{2+}$) = −1.09 V (*vs.* NHE, pH =

7). So, Ni SACs with the appropriate reduction potential can receive the photogenerated electrons from Ru to allow the CO_2-to-CO photoreduction.[41] Similarly, the LUMO energy of Bpy-PDI was calculated to be -0.84 V *vs.* NHE at pH = 7 (Fig. S11). Although the LUMO energy level of Bpy-PDI was very close to that of Ni SACs, Bpy-PDI presented quite lower catalytic properties than that of Ni SACs. This phenomenon outlined the significant role of dispersed Ni atoms in the overall catalysis.

The surface properties of Bpy-PDI and Ni SACs were investigated using N_2 and CO_2 isotherm measurements. As shown in Fig. 6a, Brunauer-Emmett-Teller (BET) surface area was increased from 2.92 $m^2\ g^{-1}$ for Bpy-PDI to 11.78 $m^2\ g^{-1}$ for Ni SACs, respectively. The type IV nitrogen adsorption-desorption isotherm indicated the existence of mesopores or macropores. Moreover, the pore width and volume of the as-prepared Ni SACs were much higher than that of pristine Bpy-PDI (Fig. S12). The characteristic properties of the special surface area and porosity could expose more catalytic sites and facilitate the contact of Ni catalysts with the reactants, thereby increasing the CO_2-to-CO photoconversion. Besides this, the incorporation of Ni atoms led to an obvious increase of the CO_2 adsorption uptake from the original 4.40 $cm^3\ g^{-1}$ for Bpy-PDI to 5.86 $cm^3\ g^{-1}$ for the Ni SACs at all relative pressures up to 1 (Fig. 6b). The larger adsorption amount of CO_2 in the catalysts suggested the selective adsorption of diluted CO_2 from gas mixtures, thereby improved catalytic activity and selectivity.

In order to investigate photoinduced charge separation and transfer process on the CO-evolution kinetics of Ni SACs, we performed electrochemical and time-resolved fluorescence (FL) emission decay spectra on Ru, Bpy-PDI and Ni SACs (Fig. 6c). FL data of Ru showed a broad emission peak centered at about 620 nm, which was attributed to the typical emission of the $[Ru(bpy)_3]Cl_2\cdot 6H_2O$ (Ru) complex.[40] The characteristic PL intensity of the Ru was suppressed greatly in the presence of Bpy-PDI, indisputably confirming that the photogenerated charge carriers of Ru were transferred and separated efficiently.[42] Notably, a lower intensity could be easily found for Ni SACs compared to that of Bpy-PDI, indicating the positive effects of Ni SACs for charge separation. In the meantime, the average lifetimes of Ru, Bpy-PDI and Ni SACs were 273.3, 248.4, and 244.9 ns, respectively (Fig. 6d). The lifetime of Ni SACs was much smaller than that of Ru and Bpy-PDI, further evidencing the dispersed Ni sites acted as the trapping sites for the capture of photoinduced electrons.[43] EIS techniques could also provide indisputable evidence to the fast separation of the photogenerated carriers.[44] As shown in Fig. S13a, Ni SACs presented a smaller arc radius in comparison with that of the Bpy-PDI samples, indicating that Ni SACs had an advantage on the migration rate of charge carriers. Besides, the polarization curves indicated that the modification of dispersed Ni atoms in Bpy-PDI could improve the current density (Fig. S13b), demonstrating the high efficiency for the charge separation and rapid surface reaction kinetics that can be acquired on Ni SACs catalysts, which was in accord with the PL results. All the above data provided indisputable evidence that the photoproduced charge carriers in Bpy-PDI modified with single Ni atoms were transferred and separated effectively, thereby improving the efficiency of redox reactions.

To track the reactive intermediates during the CO_2 photocatalytic process, in situ FTIR measurements were conducted. The signals for H_2O and CO_2 over Ni SACs increased along with the irradiation time during the CO_2 photoreduction process (Fig. 7a). The obvious bending vibration of monodentate (m-CO_3^{2-}), bidentate carbonate (b-CO_3^{2-}) and chelating-bridged carbonate (c-CO_3^{2-}) groups is recognized in Fig. 7b, indicating that Ni SACs has strong CO_2 adsorption ability. The appearance of CO_2^- at 1427 and 1683 cm^{-1} indicated that the CO_2 molecules could be well activated during the reaction.[45, 46] Furthermore, the bands at 1700, 1594, 1520, and 1375 cm^{-1} were ascribed to the characteristic stretching mode of COOH*.[47] Significantly, the characteristic COOH* adsorption peak gradually increased with illumination, indicating that the COOH* were the vital intermediates for CO_2-to-CO conversion. Interestingly, the information of intermediate CO* at 2078 cm^{-1} was figured out, further confirming the CO evolution from CO_2 photoreduction.[48, 49]

To better understand the mechanism of the outstanding catalytic performance, DFT calculations were conducted to simulate the whole catalytic reaction from the atomic level. We firstly investigated the adsorption energies of CO_2 and H_2O onto the surface of Ni SACs and Bpy-PDI, respectively. As shown in Fig. S14, the adsorbed CO_2 exhibited a bent configuration with an angle of about 141.1°, indicating the stable and linear CO_2 molecules can be effectively activated on the highly dispersed Ni atoms. The adsorption energy of CO_2 for Ni SACs was 1.44 eV (Fig. 7c), which was obviously larger than that of the Bpy-PDI (0.19 eV), indicating a much stronger adsorption affinity of single Ni catalytic sites towards CO_2. This difference in CO_2 adsorption affinity over Bpy-PDI with or without Ni SACs was in line with their CO_2 uptake results. Meanwhile, the value of H_2O adsorption energy for Ni SACs and Bpy-PDI is 0.95 eV and 0.31 eV, respectively. As is well known, the difference between CO_2 adsorption affinity and H_2O adsorption affinity is an important descriptor to comment on the CO_2 photocatalytic selectivity of different catalysts.[50] Ni SACs catalyst delivered a positive value of 0.49 eV, indicating that the CO_2 photoreduction occurred preferentially, and CO_2 adsorption may suppress the adsorption of H_2O on the Ni sites, leading to the outstanding selectivity for CO_2-to-CO conversion.[51] In contrast, the difference between CO_2 and H_2O adsorption affinity of Bpy-PDI without Ni sites was negative, showing the adverse selectivity for CO_2 reduction. The charge difference distribution illustrated the strong interaction between the Ni sites and the CO_2 molecule, which could also state that the dispersed Ni atoms were the catalytic sites for CO_2 adsorption and activation.[52] Moreover, the Bader charge of the adsorbed CO_2 molecules on the Ni sites was about 0.63 e (Fig. 7d), verifying the electron transfer from catalyst to CO_2 molecules. All these results accounted for the high performance of CO_2 photoreduction over Ni SACs, especially for diluted CO_2 reduction.

To further disclose the photocatalytic mechanism of the whole process for Ni SACs, the stepwise Gibbs free energy diagrams were calculated (Fig. 7e-f). The overall CO_2 photoreduction proceeds via the reaction pathway for CO_2 adsorption and the key intermediate of COOH* at the active single Ni sites to give the targeted CO.[7, 8] Firstly, one CO_2 molecule is captured onto the isolated Ni sites and activated to be CO*. Under light irradiation, the adsorbed CO_2 molecules accept the photoexcited electrons transferred from Ru and protons from H_2O to form COOH* intermediates. The free energy COOH* generation of Ni SACs refers to -0.07 eV, which is obviously smaller than that of Bpy-PDI (1.69 eV), indicating that the dispersed Ni atom catalyst presents a significant decrease in the energy barrier of CO_2 reduction compared to its counterpart. Then, the COOH* can be transformed into CO* by receiving another proton and electrons coupled with a dehydration process. Out of the weak bond energy of CO*, the targeted CO molecule could be easily formed and released from the surface of Ni SACs. Therefore, Ni SACs are kinetically and thermodynamically more favorable for the enhanced CO_2 photoreduction.

4. Conclusion

In conclusion, we have designed a bipyridine-based polymer by fixing single Ni atoms for photocatalytic CO_2-to-CO reduction. The as-synthesized isolated Ni catalyst enables CO_2 reduction to CO with nearly 100% selectivity in pure or diluted CO_2 conditions. This superior CO selectivity derives from the unique structure of Bpy-Ni, which functions as active sites for efficient CO_2 adsorption and activation by surpassing the binding of H_2O. Additionally, the dispersed Ni sites can reduce the reaction barrier energy and stabilize the rate-determining step of intermediates for improving CO generation. This work promotes a strategy to design and fabricate single metal atom catalyst for efficient diluted CO_2 photoreduction, showing a great significance to the practical application.

Declaration of Competing Interest

The authors declare that they have no known competing financial interests or personal relationships that could have appeared to influence the work reported in this paper.

Acknowledgements

This work was financially supported by the China Postdoctoral Science Foundation (No. 2021M701246), the National Key Research and Development Program of China (No. 2019YFC1805902, 2019YFA0210402). W.-Y. W. thanks the RGC Senior Research Fellowship Scheme (SRFS2021-5S01), the Hong Kong Research Grants Council (PolyU 15307321), Research Institute for Smart Energy (CDAQ) and Miss Clarea Au for the Endowed Professorship in Energy (847 S). In addition, we gratefully thank Beijing Synchrotron Radiation Facility at beamline 4W1B for providing us the beam time and discussion.

References

[1] J.-H. Zhang, W. Yang, M. Zhang, H.-J. Wang, R. Si, D.-C. Zhong, T.-B. Lu, Metal-organic layers as a platform for developing single-atom catalysts for photochemical CO_2 reduction, Nano Energy, 80 (2021) 105542.

[2] M. Kou, W. Liu, Y. Wang, J. Huang, Y. Chen, Y. Zhou, Y. Chen, M. Ma, K. Lei, H. Xie, P.K. Wong, L. Ye, Photocatalytic CO_2 conversion over single-atom MoN_2 sites of covalent organic framework, Appl. Catal. B, 291 (2021) 120146.

[3] J. Li, K. Li, Q. Tan, Q. Li, J. Fan, C. Wu, K. Lv, Facile preparation of highly active CO_2 reduction (001) $TiO_2/Ti_3C_2T_x$ photocatalyst from Ti_3AlC_2 with less fluorine, Catalysts, 12 (2022) 785.

[4] Y. Li, S. Wang, X.S. Wang, Y. He, Q. Wang, Y. Li, M. Li, G. Yang, J. Yi, H. Lin, D. Huang, L. Li, H. Chen, J. Ye, Facile top-down strategy for direct metal atomization and coordination achieving a high turnover number in CO_2 photoreduction, J. Am. Chem. Soc., 142 (2020) 19259-19267.

[5] H. Zhang, Y. Wang, S. Zuo, W. Zhou, J. Zhang, X.W.D. Lou, Isolated cobalt centers on $W_{18}O_{49}$ nanowires perform as a reaction switch for efficient CO_2 photoreduction, J. Am. Chem. Soc., 143 (2021) 2173-2177.

[6] S. Liang, X. Zhong, Z. Zhong, B. Han, W. Chen, K. Song, H. Deng, Z. Lin,

Biomimetic inspired porphyrin-based nanoframes for highly efficient photocatalytic CO_2 reduction, Chem. Eng. J., 411 (2021) 128414.

[7] B. Han, X. Ou, Z. Deng, Y. Song, C. Tian, H. Deng, Y.-J. Xu, Z. Lin, Nickel metal–organic framework monolayers for photoreduction of diluted CO_2: metal-node-dependent activity and selectivity, Angew. Chem. Int. Ed., 57 (2018) 16811-16815.

[8] J. Di, C. Chen, S.-Z. Yang, S. Chen, M. Duan, J. Xiong, C. Zhu, R. Long, W. Hao, Z. Chi, H. Chen, Y.-X. Weng, J. Xia, L. Song, S. Li, H. Li, Z. Liu, Isolated single atom cobalt in Bi_3O_4Br atomic layers to trigger efficient CO_2 photoreduction, Nat. Commun., 10 (2019) 2840.

[9] C. Yang, Q. Tan, Q. Li, J. Zhou, J. Fan, B. Li, J. Sun, K. Lv, 2D/2D Ti_3C_2 MXene/g-C_3N_4 nanosheets heterojunction for high efficient CO_2 reduction photocatalyst: dual effects of urea, Appl. Catal. B, 268 (2020) 118738.

[10] X. Li, K. Li, D. Ding, J. Yan, C. Wang, S.A.C. Carabineiro, Y. Liu, K. Lv, Effect of oxygen vacancies on the photocatalytic activity of flower-like BiOBr microspheres towards NO oxidation and CO_2 reduction, Sep. Purif. Technol., 309 (2023) 123054.

[11] Y. Li, Z. Ren, M. Gu, Y. Duan, W. Zhang, K. Lv, Synergistic effect of interstitial C doping and oxygen vacancies on the photoreactivity of TiO_2 nanofibers towards CO_2 reduction, Appl. Catal. B, 317 (2022) 121773.

[12] W.F. Zhong, R.J. Sa, L.Y. Li, Y.J. He, L.Y. Li, J.H. Bi, Z.Y. Zhuang, Y. Yu, Z.G. Zou, A covalent organic framework bearing single Ni sites as a synergistic photocatalyst for selective photoreduction of CO_2 to CO, J. Am. Chem. Soc., 141 (2019) 7615-7621.

[13] S. Liang, B. Han, X. Ou, X. Ye, W. Chen, H. Deng, C. Tian, Z. Lin, Lattice-strained nickel hydroxide nanosheets for the boosted diluted CO_2 photoreduction, Environ. Sci.: Nano, 8 (2021) 2360-2371.

[14] T. He, S.M. Chen, B. Ni, Y. Gong, Z. Wu, L. Song, L. Gu, W.P. Hu, X. Wang, Zirconium-porphyrin-based metal-organic framework hollow nanotubes for immobilization of noble-metal single atoms, Angew. Chem. Int. Ed., 57 (2018)

3493-3498.

[15] D. Yang, B. Ni, X. Wang, Heterogeneous catalysts with well-defined active metal sites toward CO_2 electrocatalytic reduction, Adv. Energy Mater., 10 (2020) 2001142.

[16] D. Liu, Q. He, S. Ding, L. Song, Structural regulation and support coupling effect of single-atom catalysts for heterogeneous catalysis, Adv. Energy Mater., 10 (2020) 2001482.

[17] R. Tang, X.a. Dong, J. Sheng, S. Xi, L. Zhang, F. Dong, Single-metal catalytic sites via high-throughput mechanochemistry enable selective and efficient CO_2 photoreduction, Appl. Catal. B, 316 (2022) 121661.

[18] X.-Y. Dong, Y.-N. Si, Q.-Y. Wang, S. Wang, S.-Q. Zang, Integrating single atoms with different microenvironments into one porous organic polymer for efficient photocatalytic CO_2 reduction, Adv. Mater., 33 (2021) 2101568.

[19] X. Xiong, C. Mao, Z. Yang, Q. Zhang, G.I.N. Waterhouse, L. Gu, T. Zhang, Photocatalytic CO_2 reduction to CO over Ni single atoms supported on defect-rich zirconia, Adv. Energy Mater., 10 (2020) 2002928.

[20] C. Gao, S. Chen, Y. Wang, J. Wang, X. Zheng, J. Zhu, L. Song, W. Zhang, Y. Xiong, Heterogeneous single-atom catalyst for visible-light-driven high-turnover CO_2 reduction: the role of electron transfer, Adv. Mater., 30 (2018) 1704624.

[21] L. Cheng, H. Yin, C. Cai, J. Fan, Q. Xiang, Single Ni atoms anchored on porous few-layer g-C_3N_4 for photocatalytic CO_2 reduction: the role of edge confinement, Small, 16 (2020) e2002411.

[22] B. Ravel, M. Newville, ATHENA, ARTEMIS, HEPHAESTUS: data analysis for X-ray absorption spectroscopy using IFEFFIT, J. Synchrotron Rad., 12 (2005) 537-541.

[23] G. Kresse, J. Furthmüller, Efficient iterative schemes for ab initio total-energy calculations using a plane-wave basis set, Phys. Rev. B, 54 (1996) 11169-11186.

[24] P.E. Blöchl, Projector augmented-wave method, Phys. Rev. B, 50 (1994) 17953-17979.

[25] B. Hammer, L.B. Hansen, J.K. Nørskov, Improved adsorption energetics within

density-functional theory using revised Perdew-Burke-Ernzerhof functionals, Phys. Rev. B, 59 (1999) 7413-7421.

[26] J.P. Perdew, K. Burke, M. Ernzerhof, Generalized gradient approximation made simple, Phys. Rev. Lett., 77 (1996) 3865-3868.

[27] L. Goerigk, S. Grimme, A thorough benchmark of density functional methods for general main group thermochemistry, kinetics, and noncovalent interactions, Phys. Chem. Chem. Phys., 13 (2011) 6670-6688.

[28] J.K. Nørskov, J. Rossmeisl, A. Logadottir, L. Lindqvist, J.R. Kitchin, T. Bligaard, H. Jónsson, Origin of the overpotential for oxygen reduction at a fuel-cell cathode, J. Phys. Chem. B, 108 (2004) 17886-17892.

[29] Z. Zhang, X. Chen, H. Zhang, W. Liu, W. Zhu, Y. Zhu, A highly crystalline perylene imide polymer with the robust built-in electric field for efficient photocatalytic water oxidation, Adv. Mater., 32 (2020) 1907746.

[30] G.H. Gunasekar, K. Park, V. Ganesan, K. Lee, N.-K. Kim, K.-D. Jung, S. Yoon, A covalent triazine framework, functionalized with Ir/N-heterocyclic carbene sites, for the efficient hydrogenation of CO_2 to formate, Chem. Mater., 29 (2017) 6740-6748.

[31] T.C. Zhuo, Y. Song, G.L. Zhuang, L.P. Chang, S. Yao, W. Zhang, Y. Wang, P. Wang, W. Lin, T.B. Lu, Z.M. Zhang, H-bond-mediated selectivity control of formate versus CO during CO_2 photoreduction with two cooperative Cu/X sites, J. Am. Chem. Soc., 143 (2021) 6114-6122.

[32] S. Wang, Y. Hou, X. Wang, Development of a stable $MnCo_2O_4$ cocatalyst for photocatalytic CO_2 reduction with visible light, ACS Appl. Mater. Interfaces, 7 (2015) 4327-4335.

[33] S. Liang, X. Liu, Z. Zhong, B. Han, X. Zhong, W. Chen, K. Song, H. Deng, Z. Lin, Lattice-strained nanotubes facilitate efficient natural sunlight-driven CO_2 photoreduction, Nano Res., 14 (2021) 2558-2567.

[34] B. Han, X. Ou, Z. Zhong, S. Liang, H. Deng, Z. Lin, Rational design of FeNi bimetal modified covalent organic frameworks for photoconversion of anthropogenic

CO_2 into widely tunable syngas, Small, 16 (2020) 2002985.

[35] K. Song, S. Liang, X. Zhong, M. Wang, X. Mo, X. Lei, Z. Lin, Tailoring the crystal forms of the Ni-MOF catalysts for enhanced photocatalytic CO_2-to-CO performance, Appl. Catal. B, 309 (2022) 121232.

[36] H.N. Huang, R. Shi, Z.H. Li, J.Q. Zhao, C.L. Su, T.R. Zhang, Triphase photocatalytic CO_2 reduction over silver-decorated titanium oxide at a gas-water boundary, Angew. Chem. Int. Ed., 61 (2022) e202200802.

[37] X. Wang, Z. Fu, L. Zheng, C. Zhao, X. Wang, S.Y. Chong, F. McBride, R. Raval, M. Bilton, L. Liu, X. Wu, L. Chen, R.S. Sprick, A.I. Cooper, Covalent organic framework nanosheets embedding single cobalt sites for photocatalytic reduction of carbon dioxide, Chem. Mater., 32 (2020) 9107-9114.

[38] M. Ma, Z. Huang, D.E. Doronkin, W. Fa, Z. Rao, Y. Zou, R. Wang, Y. Zhong, Y. Cao, R. Zhang, Y. Zhou, Ultrahigh surface density of Co-N_2C single-atom-sites for boosting photocatalytic CO_2 reduction to methanol, Appl. Catal. B, 300 (2022) 120695.

[39] C. Gao, Q. Meng, K. Zhao, H. Yin, D. Wang, J. Guo, S. Zhao, L. Chang, M. He, Q. Li, H. Zhao, X. Huang, Y. Gao, Z. Tang, Co_3O_4 hexagonal platelets with controllable facets enabling highly efficient visible-light photocatalytic reduction of CO_2, Adv. Mater., 28 (2016) 6485-6490.

[40] W. Chen, B. Han, C. Tian, X. Liu, S. Liang, H. Deng, Z. Lin, MOFs-derived ultrathin holey Co_3O_4 nanosheets for enhanced visible light CO_2 reduction, Appl. Catal. B, 244 (2019) 996-1003.

[41] Y.-N. Gong, W. Zhong, Y. Li, Y. Qiu, L. Zheng, J. Jiang, H.-L. Jiang, Regulating photocatalysis by spin-state manipulation of cobalt in covalent organic frameworks, J. Am. Chem. Soc., 142 (2020) 16723-16731.

[42] Y. Su, Z. Song, W. Zhu, Q. Mu, X. Yuan, Y. Lian, H. Cheng, Z. Deng, M. Chen, W. Yin, Y. Peng, Visible-light photocatalytic CO_2 reduction using metal-organic framework derived $Ni(OH)_2$ nanocages: a synergy from multiple light reflection, static charge transfer, and oxygen vacancies, ACS Catal., 11 (2020) 345-354.

[43] J. Wang, E. Kim, D.P. Kumar, A.P. Rangappa, Y. Kim, Y. Zhang, T.K. Kim, Highly durable and fully dispersed cobalt diatomic site catalysts for CO_2 photoreduction to CH_4, Angew. Chem. Int. Ed., 61 (2022) e202113044.

[44] H. Yang, D. Yang, X. Wang, POM-incorporated CoO nanowires for enhanced photocatalytic syngas production from CO_2, Angew. Chem. Int. Ed., 59 (2020) 15527-15531.

[45] X. Shi, X.a. Dong, Y. He, P. Yan, F. Dong, Light-induced halogen defects as dynamic active sites for CO_2 photoreduction to CO with 100% selectivity, Sci. Bull., 67 (2022) 1137-1144.

[46] W. Bi, L. Zhang, H. Jiang, C. Li, Y. Hu, Construction of $CuInS_2/C/TiO_2$ hierarchical tandem heterostructures with optimized CO_2 photoreduction under visible light, Chem. Eng. J., 433 (2022) 133679.

[47] F.A. Rahimi, S. Dey, P. Verma, T.K. Maji, Photocatalytic CO_2 reduction based on a Re(I)-integrated conjugated microporous polymer: role of a sacrificial electron donor in product selectivity and efficiency, ACS Catal., 13 (2023) 5969-5978.

[48] J.D. Yi, R. Xie, Z.L. Xie, G.L. Chai, T.F. Liu, R.P. Chen, Y.B. Huang, R. Cao, Highly selective CO_2 electroreduction to CH_4 by in situ generated Cu_2O single-type sites on a conductive MOF: stabilizing key intermediates with hydrogen bonding, Angew. Chem. Int. Ed., 59 (2020) 23641-23648.

[49] Z. Zhong, H. Wang, S. Liang, X. Zhong, H. Deng, Enhancing photocatalytic CO_2 reduction reaction on amorphous Ni@NiO aerogel via oxygen incorporated tuning, Appl. Catal. B, 330 (2023) 122603.

[50] B. Wentuan, L. Xiaogang, Y. Rui, C. Minglong, Y. Ruilin, H. Weixin, W. Xiaojun, C. Wangsheng, W. Changzheng, X. Yi, Surface immobilization of transition metal ions on nitrogen-doped graphene realizing high-efficient and selective CO_2 reduction, Adv. Mater., 30 (2018) 1706617.

[51] Y.H. Wu, C.J. Chen, X.P. Yan, X.F. Sun, Q.G. Zhu, P.S. Li, Y.M. Li, S.J. Liu, J.Y. Ma, Y.Y. Huang, B.X. Han, Boosting CO_2 electroreduction over a cadmium single-atom catalyst by tuning of the axial coordination structure, Angew. Chem. Int.

Ed., 60 (2021) 20803-20810.

[52] S. Zhu, X. Li, X. Jiao, W. Shao, L. Li, X. Zu, J. Hu, J. Zhu, W. Yan, C. Wang, Y. Sun, Y. Xie, Selective CO_2 photoreduction into C_2 product enabled by charge-polarized metal pair sites, Nano Lett., 21 (2021) 2324-2331.

Caption of Figures

Fig. 1 Schematic presentation of synthesis and characterizations of Ni SACs. (a) Synthetic routes of Ni SACs. (b) XRD patterns for Bpy-PDI and Ni SACs. (c) FT-IR data of Bpy-PDI and its monomers. (d) High-resolution XPS spectra of N 1s over Bpy-PDI and Ni SACs. (e) Ni 2p XPS spectrum of Ni SACs.

Fig. 2 Atomic structural characterization of Ni SACs. (a, b) Transmission electron microscopy (TEM) image of single-atom dispersed Ni SACs. (c) Aberration corrected high angle annular dark-field scanning transmission electron microscopy (HAADF-STEM) image of Ni SACs. Single Ni atoms were highlighted by yellow circles. (d-h) HAADF and corresponding elemental maps showing the distribution of C (blue), N (purple), O (red) and Ni (orange).

Fig. 3 Electronic structure characterization of Ni SACs. (a-b) XANES and corresponding EXAFS in R space at the Ni K-edge for Ni SACs and its reference samples. (c) WT pictures of NiPc, NiO, $NiCl_2$, and Ni SACs.

Fig. 4 Photocatalytic CO_2-to-CO conversion for Ni SACs. (a) Generation rate and selectivity of CO with different quality of catalyst. (b) Evolution of CO and H_2 under various reaction conditions. (c) Isotope analysis of CO using $^{13}CO_2$ and $^{12}CO_2$ as carbon sources by GC-MS. (d) Photocatalytic generation rate of CO and H_2 as a function of various CO_2 partial pressures.

Fig. 5 Optical properties and energy levels of Ni SACs. (a) UV-vis-NIR diffuse reflectance spectra, (b) Tauc plots, and (c) Mott-Schottky plot of PDA, Bpy-PDI, and Ni SACs. (d) Energy-band structure diagram of $[Ru(bpy)_3]Cl_2$ and Ni SACs for CO_2 photoreduction.

Fig. 6 Investigation of the effect for effective CO_2 photoreduction. (a) BET surface area, and (b) CO_2 uptake for Bpy-PDI and Ni SACs. (c) PL spectra and (d) time-resolved transient PL decay spectra for Ru, Bpy-PDI and Ni SACs.

Fig. 7 Detection of the catalytic mechanism for the photoreduction of CO_2 to CO. (a) In situ FTIR, and (b) amplification of partial area in panel of Ni SACs during the CO_2 photoreduction process. (c) Calculated adsorption energy of H_2O and CO_2 molecules on the Bpy-PDI and Ni site, respectively. (d) Charge density difference of CO_2 adsorption on Ni SACs. The isosurface value is set to be 0.005 e $Å^{-3}$ and cyan and yellow regions represent positive and negative charges, respectively. Δq stands for the Bader charge of adsorbed CO_2 on Ni sites. (e) Calculated free energy profile for CO_2 electroreduction on the Bpy-PDI and Ni SACs. (f) The optimized atomic structures of intermediates, and calculated free energy profile for CO_2 reduction on the Ni SACs.

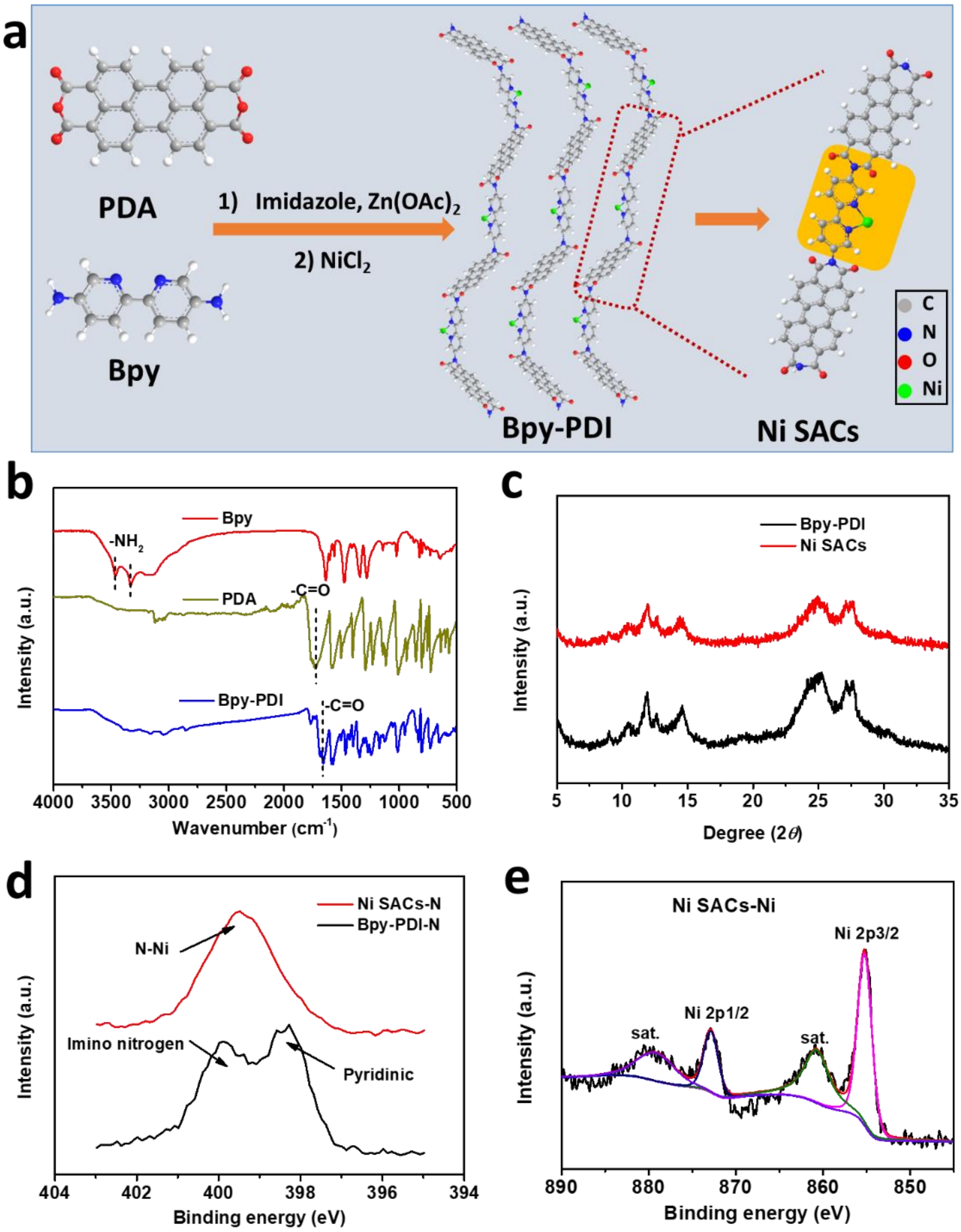

Fig. 1 Schematic presentation of synthesis and characterizations of Ni SACs. (a) Synthetic routes of Ni SACs. (b) XRD patterns for Bpy-PDI and Ni SACs. (c) FT-IR data of Bpy-PDI and its monomers. (d) High-resolution XPS spectra of N 1s over Bpy-PDI and Ni SACs. (e) Ni 2p XPS spectrum of Ni SACs.

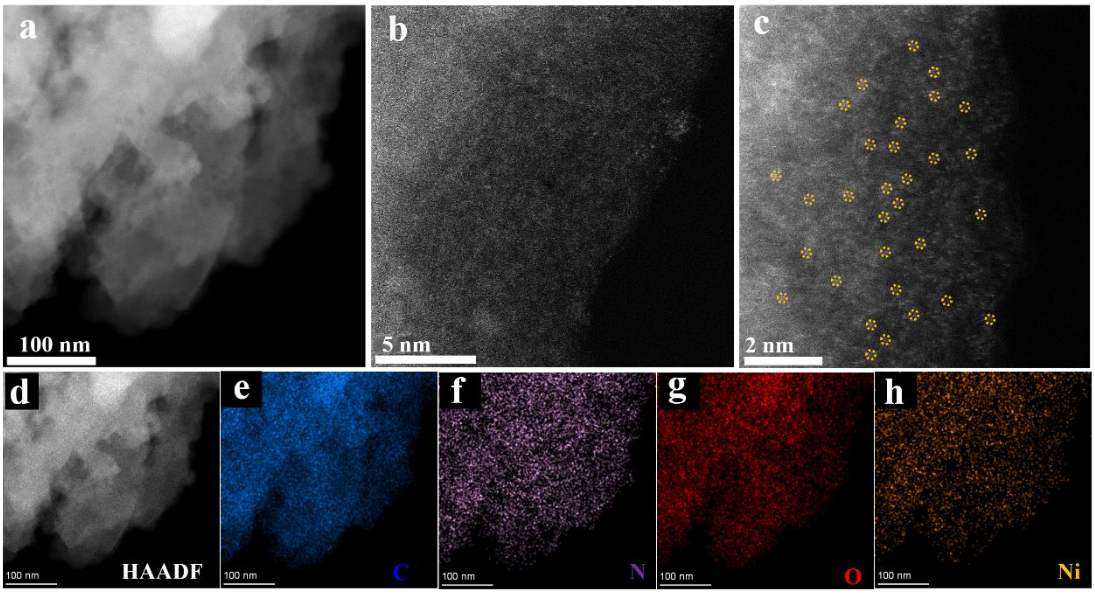

Fig. 2 Atomic structural characterization of Ni SACs. (a, b) Transmission electron microscopy (TEM) image of single-atom dispersed Ni SACs. (c) Aberration corrected high angle annular dark-field scanning transmission electron microscopy (HAADF-STEM) image of Ni SACs. Single Ni atoms were highlighted by yellow circles. (d-h) HAADF and corresponding elemental maps showing the distribution of C (blue), N (purple), O (red) and Ni (orange).

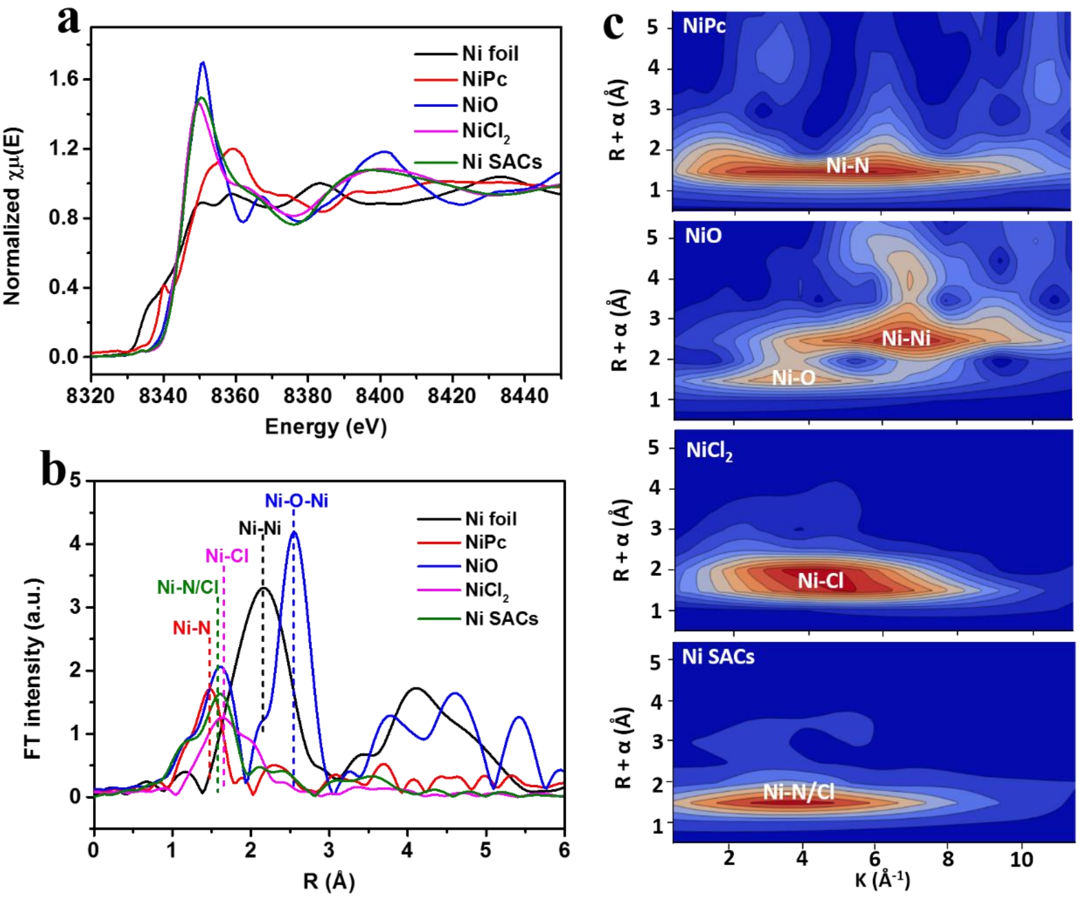

Fig. 3 Electronic structure characterization of Ni SACs. (a-b) XANES and corresponding EXAFS in R space at the Ni K-edge for Ni SACs and its reference samples. (c) WT pictures of NiPc, NiO, $NiCl_2$, and Ni SACs.

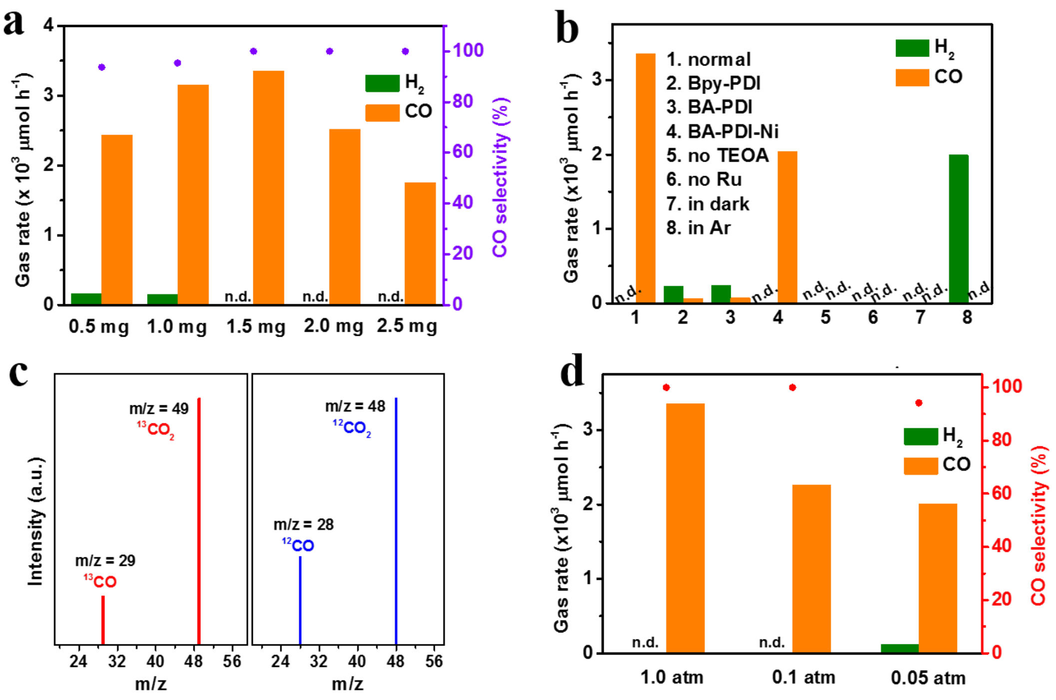

Fig. 4 Photocatalytic CO_2-to-CO conversion for Ni SACs. (a) Generation rate and selectivity of CO with different quality of catalyst. (b) Evolution of CO and H_2 under various reaction conditions. (c) Isotope analysis of CO using $^{13}CO_2$ and $^{12}CO_2$ as carbon sources by GC-MS. (d) Photocatalytic generation rate of CO and H_2 as a function of various CO_2 partial pressures.

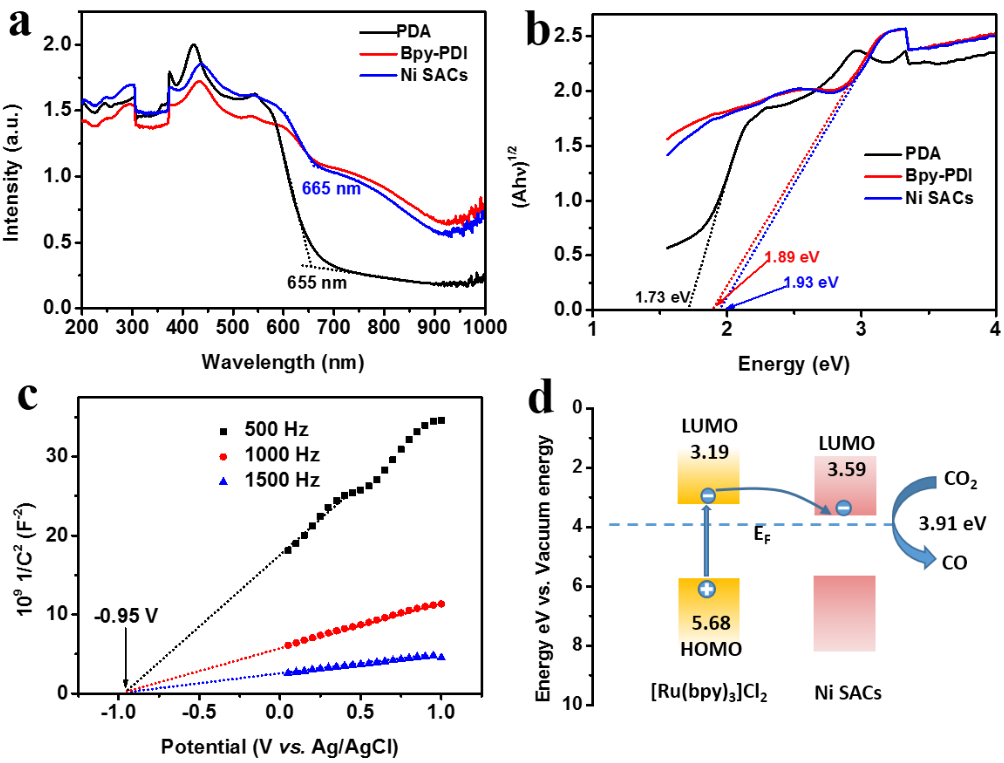

Fig. 5 Optical properties and energy levels of Ni SACs. (a) UV-vis-NIR diffuse reflectance spectra, (b) Tauc plots, and (c) Mott-Schottky plot of PDA, Bpy-PDI, and Ni SACs. (d) Energy-band structure diagram of $[Ru(bpy)_3]Cl_2$ and Ni SACs for CO_2 photoreduction.

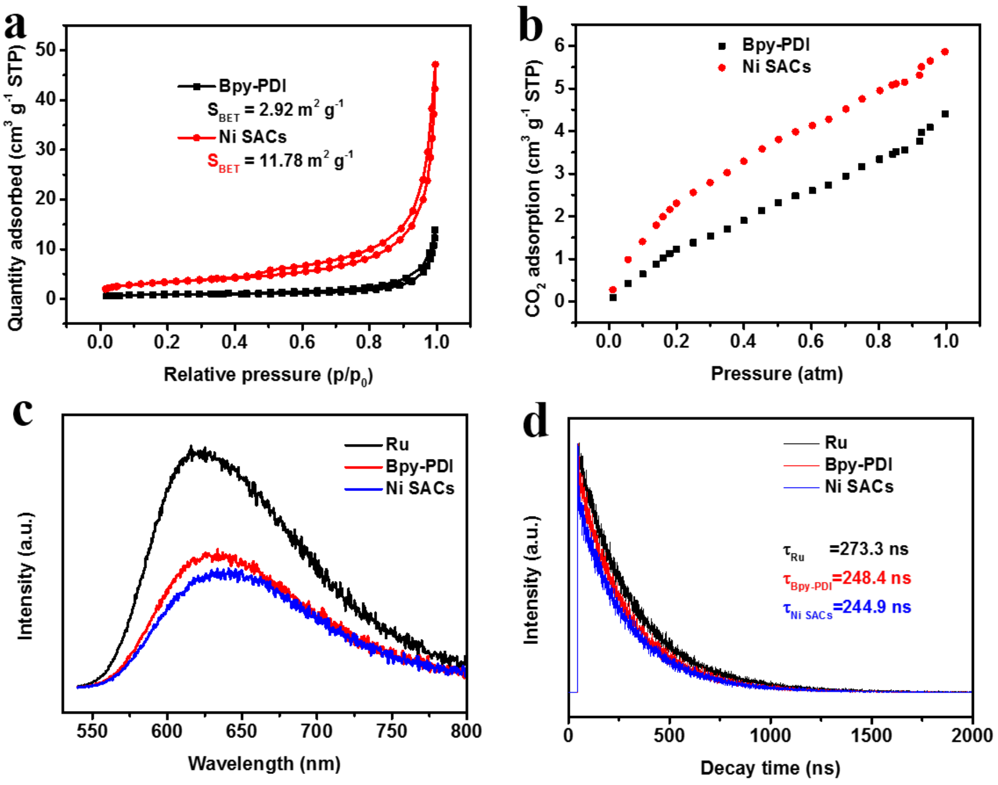

Fig. 6 Investigation of the effect for effective CO_2 photoreduction. (a) BET surface area, and (b) CO_2 uptake for Bpy-PDI and Ni SACs. (c) PL spectra and (d) time-resolved transient PL decay spectra for Ru, Bpy-PDI and Ni SACs.

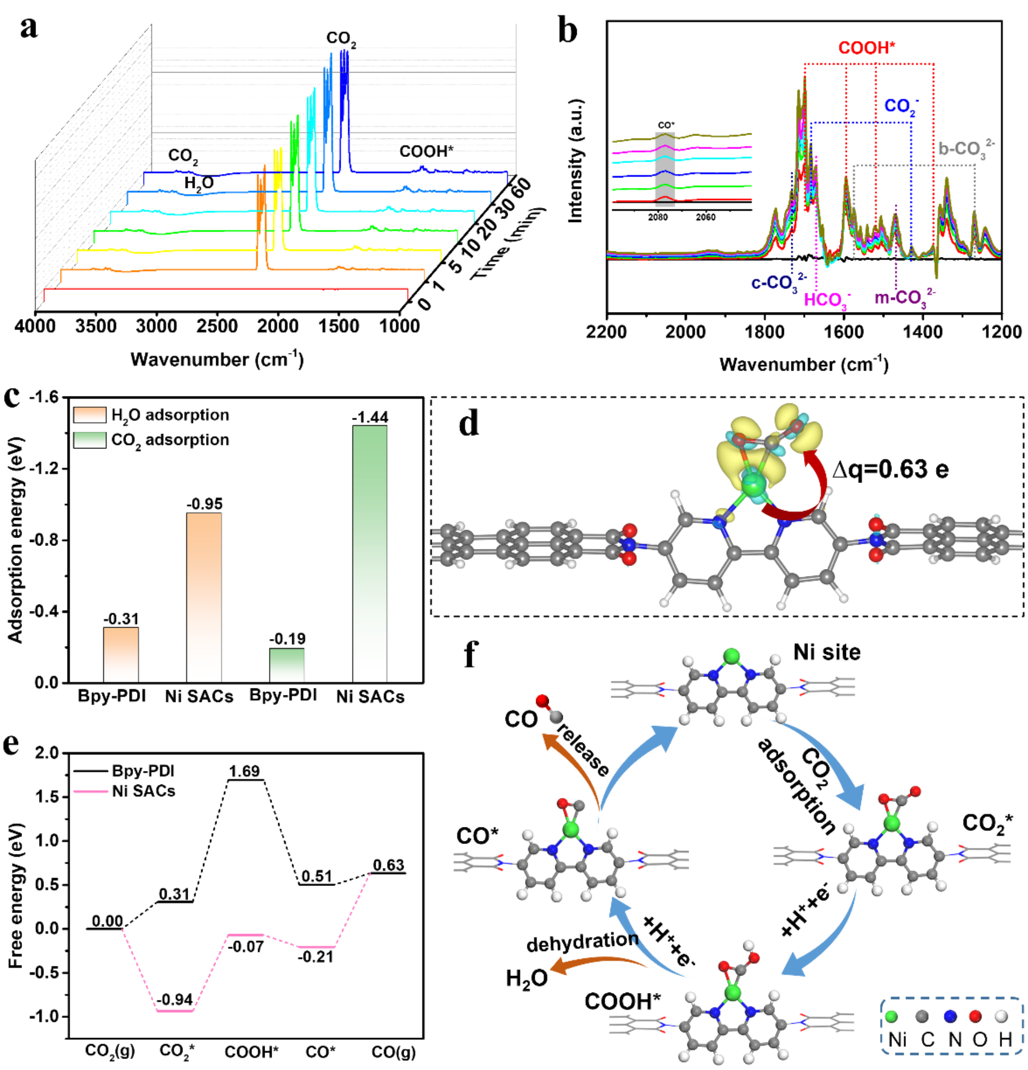

Fig. 7 Detection of the catalytic mechanism for the photoreduction of CO_2 to CO. (a) In situ FTIR, and (b) amplification of partial area in panel of Ni SACs during the CO_2 photoreduction process. (c) Calculated adsorption energy of H_2O and CO_2 molecules on the Bpy-PDI and Ni site, respectively. (d) Charge density difference of CO_2 adsorption on Ni SACs. The isosurface value is set to be 0.005 e $Å^{-3}$ and cyan and yellow regions represent positive and negative charges, respectively. Δq stands for the Bader charge of adsorbed CO_2 on Ni sites. (e) Calculated free energy profile for CO_2 electroreduction on the Bpy-PDI and Ni SACs. (f) The optimized atomic structures of intermediates, and calculated free energy profile for CO_2 reduction on the Ni SACs.